A 2D Unified (Non-) Hydrostatic Model of the Atmosphere with a Discontinuous Galerkin Method

Matthias Läuter[a1], Francis X. Giraldo[b], Sebastian Reich[c], Marco Restelli[d], Dörthe Handorf[a], Klaus Dethloff[a]

a Alfred Wegener Institute for Polar and Marine Research in the Helmholtz Association, P.O. Box 60 01 49, 14401 Potsdam, Germany
b Naval Postgraduate School, Department of Applied Mathematics, Spanagel Hall 262, 833 Dyer Road, Monterey, CA 93943-5216, USA
c Universität Potsdam, Institute of Mathematics, University Potsdam, Am Neuen Palais 10, 14469 Potsdam, Germany
d Ecuaciones Diferenciales y Análisis Numérico, Universidad de Sevilla, Facultad de Matemáticas, C/ Tarfia s/n, 41012 Sevilla, Spain

Abstract

A two dimensional mesoscale atmospheric model is presented based on two systems of dynamical equations, the non-hydrostatic compressible Euler equations and the corresponding hydrostatic system. Both equation systems are discretized with a discontinuous Galerkin method in space and a linear semi-implicit multistep method in time. To cover elementwise polynomial spaces up to order four, exact quadrature rules are used. The method is applied to a terrain following quadrilateral grid. To validate the models, gravity wave propagation and mountain wave experiments are analyzed. The numerical models exhibit the proper wave propagation characteristics and high order convergence rates.

1 Introduction

The compressible Euler equations, or the non-hydrostatic equation system, are the governing equations for atmospheric motion of adiabatic dry and frictionless air. They cover important dynamical features of atmospheric fluid motion, their dynamics is extremely non-linear and characterized by interactions between processes of multiple spatial and temporal scales. The presence of sound waves, the potential for the development of energetic shocks, and the potential for wave breaking and scale collapses are fundamental features of these equations. Sound waves are the fastest waves contained in these equations and usually constitute a severe CFL-condition for the explicit time step size according to linear stability analysis. Thus, filtering the dynamical equations to exclude sound wave propagation is one way to circumvent this problem. E.g. incompressible, anelastic and pseudo-incompressible equations do not contain fast sound waves, see e.g. Ogura and Phillips (1962), Durran (1989). The hydrostatic approximation leads to a vertically filtered system, but allows horizontally propagating fast Lamb waves, see e.g. Kalnay (2003). This is

[1]E-Mail: Matthias{dot}Laeuter{at}awi{dot}de (Matthias Läuter)

one reason why for several decades, the hydrostatic system was used for weather forecast and climate simulations. Another way to avoid strict CFL-conditions is to consider the unfiltered equation system and to use implicit or semi-implicit time integration schemes with larger stability regions appropriate for stiff problems.
Within the present article, we consider examples for both types of equations. These are the unfiltered fully non-hydrostatic system and the vertically filtered hydrostatic system. For these two systems we analyze wave propagation characteristics caused by initial perturbations and mountain wave forcings. Specifically, this analysis estimates the range of horizontal scales that is properly represented within the hydrostatic equation system. It should be noted that constructing a hydrostatic model based on a discontinuous Galerkin method is a mathematically challenging problem that we show here how to solve in a mathematically consistent approach. Further, our interest is to present a detailed convergence study to compare experimental and theoretical spatial convergence rates. To our knowledge, this has never been shown before for either hydrostatic or non-hydrostatic atmospheric models. For 2-dimensional mesoscale atmospheric models, a number of experimental setups are known from the literature. Skamarock and Klemp (1994) studied the propagation of inertia gravity waves in non-hydrostatic and hydrostatic setups. Meanwhile Pinty *et al.* (1995) give examples for single mountains with hydrostatic and non-hydrostatic shape size and Schär *et al.* (2002) propose multiple mountains in a consecutive formation.
In our current paper, we discretize the equations in space with the discontinuous Galerkin method (DGM), one possible high order generalization of finite volume methods. Since the DGM was proposed in the early 1970s in Reed and Hill (1973), it has become a powerful computational tool for inviscid and viscous problems in gas dynamics. For atmospheric applications Giraldo *et al.* (2002), Nair *et al.* (2005), Giraldo (2006), Giraldo and Restelli (2008), Läuter *et al.* (2008) and Restelli and Giraldo (2009) have successfully applied the DGM. It features high order accuracy, discrete conservation properties, applicability on structured and unstructured grids, and robustness especially for non-linear problems. The locality of memory usage offers very good scalability on multi-core architectures and on graphics processors, see e.g. Biswas *et al.* (1994) and Klöckner *et al.* (2009).
Giraldo and Restelli (2008) and Restelli and Giraldo (2009) have presented a DGM solving the non-hydrostatic system in a mesocale atmospheric channel on a rectangular grid. The grid is deformed into the vertical direction to obtain a terrain following grid structure. The temporal evolution of the conserved variables is computed solving a system of conservation laws. For the hydrostatic equations, the situation is different because the vertical momentum component is no longer prognostic. Further, these equations consist of the conservation laws for the remaining prognostic variables with the hydrostatic constraint to determine the diagnostic vertical momentum W as a Lagrangian multiplier. For the conservation laws, the DGM is applied using the standard Rusanov numerical flux. For the hydrostatic equations this numerical flux is modified considering jump contributions of W only into the vertical direction. Our approach shows that the non-hydrostatic and hydrostatic equations can be implemented in a unified way and their differences are controlled by a hydrostatic switch parameter δ_H. As described above semi-implicit (implicit-

explicit) time discretization schemes offer improved stability properties and lead to larger time steps even for stiff systems containing fast waves. For the DGM Dolejsi and Feistauer (2004), Kanevsky *et al.* (2007), Giraldo and Restelli (2009) and Restelli and Giraldo (2009) have shown the successful application of semi-implicit Runge-Kutta methods and linear multi-step methods. In our current work for both systems, the non-hydrostatic and hydrostatic, a 2nd order semi-implicit linear multi-step method is chosen that combines robust stability and high order properties in time.
The article is structured the following way. After the introduction of the non-hydrostatic and hydrostatic systems in section 2, section 3 describes the DGM and the temporal scheme for both equation systems. In section 4 the experimental results including a convergence study are presented. Finally, in section 5 we summarize the main results and propose future work.

2 Non-Hydrostatic and Hydrostatic Systems

In this section the governing dynamical equations are discussed representing the mathematical model describing the atmospheric flow problems considered in this article. Two different systems of equations for compressible dry inviscid air with gravitational acceleration will be considered, the non-hydrostatic and hydrostatic equation system.
Because our approach is to apply a discontinuous Galerkin method to the equations, we restrict our attention to equations in conservation/flux form. Two flux formulations of the non-hydrostatic system are known: one uses density, momentum and potential temperature (the Θ-formulation) and the other uses density, momentum and total energy as prognostic variables. For the hydrostatic approximation, the prognostic equation for the vertical momentum W is modified into a diagnostic one. As a consequence, the kinetic and total energy equations lose their prognostic structure whereas the potential temperature equation remains prognostic. Because of this observation, we restrict ourselves to the Θ-formulation of the non-hydrostatic system.
The governing equations will be considered in the 2-dimensional spatial domain

$$\Omega = \{(x, z) \in (x_L, x_R) \times \mathbb{R} \,|\, z_B(x) < z < z_T\}$$

where $x_L < x_R$ are the x-components of the left and right boundary. $z_B : (x_L, x_R) \to \mathbb{R}$ is a given height function describing the domain bottom orography and z_T is the z-component of the rigid lid on top. In Ω, we will denote coordinates by (x_1, x_2) and (x, z) depending on the context.

2.1 Physical Variables

The non-hydrostatic system and its hydrostatic approximation are given by

$$\Delta_H \partial_t q + \operatorname{div} f(q) = r(q) \quad \text{in} \quad \Omega \times \mathbb{R}_{>0} \tag{1}$$

with the conserved variables $q = (\rho, U, W, \Theta)^{\mathrm{T}} = (\rho, \rho u, \rho w, \rho\theta)^{\mathrm{T}}$, density ρ, the velocity vector (u, w), the potential temperature θ and the time domain $\mathbb{R}_{>0} = \{t \in \mathbb{R} \,|\, t > 0\}$. The flux function and the right hand side are defined by

$$f(q) = \begin{pmatrix} U & W \\ \frac{U^2}{\rho} + p & \frac{UW}{\rho} \\ \delta_H \frac{UW}{\rho} & \delta_H \frac{W^2}{\rho} + p \\ \theta U & \theta W \end{pmatrix}, \quad r(x, z, q) = \begin{pmatrix} \sigma(\rho_\sigma - \rho) \\ \sigma(U_\sigma - U) \\ -\rho g - \delta_H \sigma W \\ \sigma(\Theta_\sigma - \Theta) \end{pmatrix},$$

$$\Delta_H = \begin{pmatrix} 1 & 0 & 0 & 0 \\ 0 & 1 & 0 & 0 \\ 0 & 0 & \delta_H & 0 \\ 0 & 0 & 0 & 1 \end{pmatrix}$$

with the pressure $p = c_0 \Theta^\gamma$, $c_0 = (R/p_0^\kappa)^\gamma$, the gas constant R, a constant pressure p_0, the isentropic exponent γ, the Poisson constant κ and the gravitational constant g. $\sigma(x, z) \geq 0$ is the prescribed Raleigh damping parameter and ρ_σ, U_σ, Θ_σ the corresponding fields that realize the non-reflecting boundary within a sponge layer, see section 4. For the parameter switch $\delta_H = 1$, Eq. (1) describes the non-hydrostatic system, for $\delta_H = 0$ these are the equations in hydrostatic approximation.

2.2 Perturbation Variables

To enhance the hydrostatic equilibrium of the model the numerical method will be applied to the perturbation variable with respect to a reference field. For that we assume a hydrostatic reference field $q_r = (\rho_r = \rho_\sigma, 0, 0, \Theta_r = \Theta_\sigma)^{\mathrm{T}}$, $p_r = c_0 \Theta_r^\gamma$, $\theta_r = \frac{\Theta_r}{\rho_r}$ with the properties $\partial_z p_r = -g\rho_r, \quad \partial_t q_r = 0, \quad \partial_x q_r = 0$. The choice for the reference fields depends on the numerical experiment and will be reported in section 4. Defining the perturbation variables

$$q' = q - q_r, \quad p'(z, q') = p(q_r(z) + q') - p_r(z),$$

system (1) can be formulated in terms of q' by

$$\Delta_H \partial_t q' + \operatorname{div} f'(z, q') = r(q') \quad \text{in} \quad \Omega \times \mathbb{R}_{>0} \tag{2}$$

with

$$f'(z, q') = \begin{pmatrix} U & W \\ \frac{U^2}{\rho} + p' & \frac{UW}{\rho} \\ \delta_H \frac{UW}{\rho} & \delta_H \frac{W^2}{\rho} + p' \\ \theta U & \theta W \end{pmatrix}, \quad r(x, z, q') = \begin{pmatrix} -\sigma\rho' \\ \sigma(U_\sigma - U) \\ -g\rho' - \delta_H \sigma W \\ -\sigma\Theta' \end{pmatrix}.$$

To simplify the notation for the rest of the article, we omit the primes.

3 Conservative Numerical Method

To approximate the spatial derivatives of the dynamical equations (2), we consider a discontinuous Galerkin method on a logically rectangular grid combined with a

second order semi-implicit backward difference time step method. The grid geometry is defined by a terrain following σ_z-coordinate giving a deformation into the vertical direction. Using the concept of isoparametric finite elements, the discrete function space consists of high order tensor product polynomials in each element. Based on an integral form of the equation system, a high order discontinuous Galerkin method is defined. Thus, the conservation properties for the conserved variables are assigned to the discrete variables.

3.1 Terrain following Grid

The numerical method is based on a rectangular computational grid based on a terrain following σ_z-coordinate. This vertical coordinate with a linear decay of terrain slopes, see e.g. Gal-Chen and Somerville (1975), is defined by a global coordinate mapping

$$\gamma : O \to \Omega, \quad \gamma(x,z) = \left(x, z_B(x)\frac{z_T - z}{z_T} + z \right)$$

from the computational domain $O = (x_L, x_R) \times (0, z_T)$ to the spatial domain Ω. For the horizonal and vertical element numbers N_x and N_z, a rectangular grid structure is defined on O by the supporting points

$$x_L = x_0 < x_1 < .. < x_{N_x} = x_R, \quad 0 = z_0 < z_1 < .. < z_{N_z} = z_T.$$

For each index $(i,j) = \{1,..,N_x\} \times \{1,..,N_z\}$ the computational and its corresponding spatial element are defined by

$$E_{c,ij} = (x_{i-1}, x_i) \times (z_{j-1}, z_j), \quad E_{ij} = \gamma(E_{c,ij}),$$

such that Ω is covered by all elements

$$\overline{\Omega} = \bigcup_{E \in \mathcal{T}} \overline{E}$$

of the grids triangulation $\mathcal{T} = \{E_{ij}\}_{i=1,..,N_x, j=1,..,N_z}$.

3.2 Discontinuous Galerkin Method

On each element $E \in \mathcal{T}$ with respect to the reference element $E_c \subset O$, the isoparametric tensor product polynomial space of degrees at most $k \geq 1$ is defined by

$$\begin{aligned} Q^k(E) &= \{\varphi : E \to \mathbb{R} \,|\, \varphi \circ \gamma|_{E_c} \in Q_c^k(E_c)\}, \\ Q_c^k(E_c) &= \text{span}\{p_{ij} : E_c \to \mathbb{R} \,|\, 0 \leq i,j \leq k; p_{ij}(x,z) = x^i z^j\}. \end{aligned}$$

We notice the dimension of the polynomial space to be $N_k = \dim Q^k(E) = (k+1)^2$ and the set of integer numbers $\bar{N}_k = \{1,..,N_k\}$. Thus, the coordinate mapping γ defines both the geometry of the element E and the polynomial space on E. Based

on the polynomial space $Q^k(E)$, the discrete discontinuous function space is defined by

$$V = \{\varphi \in L^\infty(\Omega) \,|\, \varphi|_E \in Q^k(E), \quad \forall E \in \mathcal{T}\}.$$

Because $\varphi \in V$ are polynomials on each grid element $E \in \mathcal{T}$, the condition $\varphi \in L^\infty$ does not constitute an additional constraint to the discrete functions.
The starting point for the space-discrete formulation is an appropriate integral form of the dynamic equations (2). This is obtained multiplying (2) with a smooth (continuous in Ω with derivatives) test function $\Phi : \Omega \to \mathbb{R}^4$, assuming a smooth solution q of (2), integrating over each $E \in \mathcal{T}$ and applying integration by parts, that is

$$\int_E \Phi \cdot \Delta_H \partial_t q - f : \nabla\Phi \, dx + \int_{\partial E} \Phi \cdot (f\nu_E) \, d\sigma = \int_E \Phi \cdot r \, dx.$$

Assuming the indices $i = 1, 2$ and $j = 1, .., 4$, the terms are defined by $f : \nabla\Phi = \sum_{i,j} f_{ij} \partial_{x_j} \Phi_i$, $\Phi \cdot (f\nu_E) = \sum_{i,j} \Phi_i f_{ij} \nu_{E,j}$ and $\nu_E \in \mathbb{R}^2$ is the normal vector outward on ∂E. The discrete version of this integral form gives the discontinuous Galerkin method, the condition that the space-discrete solution $q(., t) \in V^4$ has to fulfill, namely

$$(\Delta_H \partial_t q, \Phi)_{L^2(\Omega)} + F(q(., t), \Phi) = 0 \quad \text{for all} \quad \Phi \in V^4 \tag{3}$$

with the discontinuous Galerkin operator $F(q, \Phi) = \sum_{E \in \mathcal{T}} F_E(q, \Phi)$ for $\operatorname{div} f(q) - r(q)$ and

$$F_E(q, \Phi) = -\int_E f : \nabla\Phi + \Phi \cdot r \, dx + \int_{\partial E} \Phi_{in} \cdot \hat{f}(z, q_{in}, q_{out}, \nu_E) \, d\sigma. \tag{4}$$

Because the values of q are not uniquely defined on ∂E, inner and outer values q_{in} and q_{out} are considered and the flux function is substituted by a numerical flux function $\hat{f}$. For the boundary integral along ∂E, at the element boundary point $x_0 \in \partial E$, the inner value is defined by

$$q_{in}(x_0) = \lim_{x \in E, x \to x_0} q(x).$$

For an inner element edge point $x_0 \in \partial E \setminus \partial\Omega$ respectively a boundary edge point $x_0 \in \partial E \cap \partial\Omega$, the outer value is defined by

$$q_{out}(x_0) = \lim_{x \in \Omega \setminus E, x \to x_0} q(x) \quad \text{resp.} \quad q_{out}(x_0) = \lim_{x \in E, x \to x_0} \begin{pmatrix} \rho \\ \begin{pmatrix} U \\ W \end{pmatrix} - 2 \begin{pmatrix} U \\ W \end{pmatrix} \cdot \nu \, \nu \\ \Theta \end{pmatrix}.$$

This way, reflecting boundary conditions on $\partial\Omega$ are prescribed for the flow. For the boundary integral in (4), a numerical flux function replaces the flux $f(q)$. Among the different choices for the numerical flux, we have taken the Rusanov numerical flux

$$\hat{f}(z, q_1, q_2, \nu) = \frac{1}{2} \left[f(z, q_1)\nu + f(z, q_2)\nu - \lambda(\Delta_H \nu_x^2 + \mathrm{Id}_4 \, \nu_z^2)(q_2 - q_1) \right] \tag{5}$$

where we have used the decomposition $\nu = (\nu_x, \nu_z)$ and Id_4 is the rank-4 identity matrix. Because for the hydrostatic case $\delta_H = 0$ the vertical momentum jumps are weighted with ν_z^2, this term vanishes along vertically aligned element faces. To represent the space-discrete solution $q(.,t) \in V^4$ of the discontinuous Galerkin method (3), a basis of V is specified. For that, in each element $E \in \mathcal{T}$, a Lagrangian basis $(\varphi_{E,i})_{i\in\bar{N}_k}$ is defined with respect to a tensor product Gauss-Lobatto points as collocation points, see Bos *et al.* (2000). Let us continue each basis function $\varphi_{E,i} : E \to \mathbb{R}$ by zero to the whole domain Ω and denote this discontinuous function again by $\varphi_{E,i}$. Then, $(\varphi_{E,i})_{E\in\mathcal{T},i\in\bar{N}_k}$ establishes a Lagrangian basis of V. Now, each scalar component q_l of the discrete solution q can be represented with respect to this basis, that is

$$q_l(x,z,t) = \sum_{i=1}^{N_k} q_{l,E,i}(t)\varphi_{E,i}(x,z),$$

with the components $q_{l,E,i}$ and the component vector $\bar{q} = (q_{l,E,i})_{E\in\mathcal{T};l=1,..,4;i\in\bar{N}_k}$. Applying this to (3) yields the quasilinear differential algebraic system

$$M_H \frac{d\bar{q}}{dt} + \bar{F}(\bar{q}) = 0, \quad M_H = \begin{pmatrix} M & 0 & 0 & 0 \\ 0 & M & 0 & 0 \\ 0 & 0 & \delta_H M & 0 \\ 0 & 0 & 0 & M \end{pmatrix} \tag{6}$$

with the mass matrix $M = (\int_\Omega \varphi_{E,i}\varphi_{F,j})_{(E,i),(F,j)\in\mathcal{T}\times\bar{N}_k}$ and the appropriate vector function $\bar{F}$. For the non-hydrostatic system ($\delta_H = 1$), (6) simplifies to a system of ordinary differential equations by inverting the mass matrix M_H.
The construction of the vector $\bar{F}$ includes $F_E(q,\Phi)$ in (4) and further the evaluation of integrals over E and ∂E. This is done applying appropriate quadrature rules. For that, we follow Cockburn and Shu (2001) to obtain $k+1$-order formal accuracy and consider tensor Gauss-Lobatto quadrature rules of order $2k$ in each element E. On each edge of E, Gauss-Lobatto rules of order $2k+1$ are applied that imply the evaluation of the integrand at the quadrature points, and differ from the collocations points of the Lagrange polynomial basis.

3.3 Semi-Implicit Linear Multistep Method

One possibility to discretize the semi-discrete problem (6) is a linear multistep method. Due to advection terms and the non-linear wave speed λ in the Rusanov flux, the discontinuous Galerkin operator $\bar{F}$ is non-linear. Although Newton-type solvers for this non-linear problem are a possible choice, numerical efficiency is still an open problem. Here, a semi-implicit (or implicit-explicit) multistep method is chosen, to take advantage of a large stability region, see Hundsdorfer and Verwer (2003), Giraldo (2005), Giraldo *et al.* (2009). Further, the hydrostatic constraint can be enforced implicitly in every time step; this (along with the flux function defined in (5)) is the key to constructing a mathematically-consistent discontinuous Galerkin method for the hydrostatic equations.
To apply the semi-implicit method, a linear discontinuous Galerkin operator $\bar{L}$ is introduced to approximate $\bar{F}$. In section 3.2, the non-linear operator $\bar{F}$ is constructed

based on the flux function f. Now, the same procedure is chosen to construct $\bar{L}$ based on a linearized flux function l. With the hydrostatic reference fields ρ_r, θ_r, Θ_r in section 2.2, a Taylor approximation of f yields

$$l(z,q) = \begin{pmatrix} U & W \\ p_l & 0 \\ 0 & p_l \\ \theta_r U & \theta_r W \end{pmatrix}, \quad p_l(z,\Theta) = c_0 \gamma \Theta_r^{\gamma-1}(z)\Theta.$$

With respect to l a linear discontinuous Galerkin operator for $\operatorname{div} l(q) - r(q)$ is defined by

$$L(q,\Phi) = \sum_{E\in\mathcal{T}} -\int_E l : \nabla\Phi + \Phi \cdot r \, dx + \int_{\partial E} \Phi_{in} \cdot \hat{l}(z, q_{in}, q_{out}, \nu_E) \, d\sigma$$

with a constant speed of sound $\lambda_0 > 0$ and the linear Rusanov numerical flux

$$\hat{l}(z,q_1,q_2,\nu) = \frac{1}{2}\left[l(z,q_1)\nu + l(z,q_2)\nu - \lambda_0(\Delta_H \nu_x^2 + \mathrm{Id}_4\, \nu_z^2)(q_2 - q_1)\right].$$

Different to the Rusanov flux in (5), the wave speed λ_0 is a constant and ensures the linearity of the numerical flux $\hat{l}$. Finally, the linear operator $\bar{L}$ is constructed from $L(q,\Phi)$ applying the representation of the Lagrangian basis of V. Now, the differential algebraic system (6) can be rewritten with a linear $\bar{L}$ and a non-linear $\bar{F} - \bar{L}$, that is

$$M_H \frac{d\bar{q}}{dt} + \bar{L}(\bar{q}) + (\bar{F} - \bar{L})(\bar{q}) = 0.$$

For the temporal discretization, the second order semi-implicit backward difference formula BDF2, a linear 3-step method, is used treating $\bar{L}$ implicitly and $\bar{F} - \bar{L}$ explicitly, see Giraldo and Restelli (2009). For each time step $t^n \to t^{n+1}$ this can be written as

$$M_H\left(\bar{q}^{n+1} - \sum_{m=0}^{1} \alpha_m \bar{q}^{n-m}\right) + \eta\Delta t \sum_{m=0}^{1} \beta_m (\bar{F} - \bar{L})(\bar{q}^{n-m}) + \eta\Delta t \bar{L}(\bar{q}^{n+1}) = 0 \quad (7)$$

with the parameters $\alpha_0 = \frac{4}{3}$, $\alpha_1 = -\frac{1}{3}$, $\eta = \frac{2}{3}$, $\beta_0 = 2$ and $\beta_1 = -1$. Giraldo and Restelli (2009) have further studied a set of higher order implicit BDFs, which would be desirable for an high order application. But, because the stability regions of the higher order BDFs do exclude a neighborhood of 0 on the imaginary axis, these alternatives tend to generate instabilities.

The linear operator $\bar{L}$ is chosen, such that the implicit operator $\bar{L}$ includes the fast/sound waves and explicit operator $\bar{F} - \bar{L}$ the advective waves. The A-stability of the implicit part of the BDF circumvents a time step restriction. But to obtain linear stability, the explicit part of the BDF method causes a maximum CFL-timestep Δt_{ad} with respect to the advective wave speed. Because in section 4 we concentrate on accuracy rather than on stability, the time steps used for the experiments are

far below the stability limit Δt_{ad}. To control the model time step, we define a characteristic time that takes the sound waves to pass a grid element, that is

$$\Delta t_{so} = \frac{\Delta x}{c_{so}(2k+1)} \tag{8}$$

with the sound wave speed $c_{so} = \sqrt{u^2+w^2} + \sqrt{\gamma p/\rho}$. The motivation for this choice is the CFL-condition in Cockburn and Shu (2001) for explicit Runge-Kutta Discontinuous-Galerkin methods both of order $k+1$ applied to the one-dimensional linear case.

3.4 Discrete Hydrostatic Balance

Both options $\delta_H = 0$ and $\delta_H = 1$ have been considered with a backward differencing formula in the last section. For the non-hydrostatic case, Eq. (7) recovers the approach of Restelli and Giraldo (2009) but for the energy form of the Euler equations.
The hydrostatic system case with $\delta_H = 0$ has a different structure. While, the equations for ρ, U and Θ in (7) remain the same, the third equation in (7) does not include a discrete time derivative for $\partial_t W$. How does this equation look like? To answer this question, we consider the test function $\Phi = (0, 0, \varphi, 0)$ and observe

$$(F-L)(q,\Phi) = \sum_{E\in\mathcal{T}} -\int_E (p-p_l)\partial_z\varphi\,dx + \int_{\partial E} \varphi_{in}(\hat{p}-\hat{p}_l)\nu_{E,z}\,d\sigma,$$
$$L(q,\Phi) = \sum_{E\in\mathcal{T}} -\int_E p_l\partial_z\varphi - g\rho\varphi\,dx + \int_{\partial E} \varphi_{in}\hat{p}_l\nu_{E,z}\,d\sigma$$

where $\hat{p}$ and $\hat{p}_l$ are the values of the pressure functions on the element boundary defined by the Rusanov numerical fluxes. Applying this to (7) for all $E \in \mathcal{T}$ and $\varphi \in V$ yields

$$-\int_E (\sum_{m=0}^{1} \beta_m (p-p_l)^{n-m} + p_l^{n+1})\partial_z\varphi\,dx$$
$$+\int_{\partial E} (\sum_{m=0}^{1} \beta_m (\hat{p}-\hat{p}_l)^{n-m} + \hat{p}_l^{n+1})\varphi\nu_{E,z}\,d\sigma = -\int_E g\rho^{n+1}\varphi\,dx.$$

Provided the temporal truncation error can be neglected

$$p^{n+1} = \sum_{m=0}^{1} \beta_m (p-p_l)^{n-m} + p_l^{n+1} + \mathcal{O}(\Delta t^2),$$

the third equation in (7) can be considered as a discrete hydrostatic balance at time t^{n+1}, namely

$$-\int_E p^{n+1}\partial_z\varphi\,dx + \int_{\partial E} \hat{p}^{n+1}\varphi\nu_{E,z}\,d\sigma = -\int_E g\rho^{n+1}\varphi\,dx. \tag{9}$$

In other words, Eq. (9) is the conservative discontinuous Galerkin representation of the hydrostatic balance.

4 Model Validation

The experimental results presented within this section will show the applicability of the discontinuous Galerkin method to the non-hydrostatic and hydrostatic systems. Characteristic wave features can be established and convergence studies show the expected convergence rates for smooth numerical solutions. The experiments are performed for the polynomial orders $k = 1, 2, 3, 4$, with the linear semi-implicit multistep method BDF2.
For each model experiment, the model resolution is given by a number $h_\beta > 0$. Depending on the anisotropy parameter $\beta > 0$, h_β reflects different resolutions into the horizontal and vertical direction. To specify this, the anisotropic element size of $E \in \mathcal{T}$, the anisotropic grid size and the anisotropic model resolution are defined by

$$|E|_\beta = \max(\max_{(x_0,z_0),(x_1,z_1)\in E} |x_0 - x_1|, \beta \max_{(x_0,z_0),(x_1,z_1)\in E} |z_0 - z_1|),$$
$$\Delta x_\beta = \max_{E\in\mathcal{T}} |E|_\beta, \quad h_\beta = \frac{\Delta x_\beta}{k+1},$$

with the polynomial order k. This way, a grid with $h = 10$km and $\beta = 2$ effectively has a horizontal resolution of 10km and a vertical resolution of 5km. We will write h instead of h_β if the assignment is clear.

4.1 Gravity Waves

The first validation test is a gravity wave caused by an initial potential temperature perturbation θ' of an uniformly stratified atmosphere. Following Giraldo and Restelli (2008) for the potential temperature θ, the initial condition is $\theta_r + \theta'$ with the reference field $\theta_r(z) = \theta_0 \exp(N^2 z/g)$, the Brunt-Väisälä frequency $N = 0.01\,\mathrm{s}^{-1}$, the temperature constant $\theta_0 = 300$K and the horizontal velocity $u = 20$m/s. The initial perturbation is given by

$$\theta'(x,z) = \Delta\theta_0 \sin(lz) A(a, x_c, x) \tag{10}$$

with $\Delta\theta_0 = 0.01$K, $l = \pi/10$km, the Agnesi "versiera" mountain profile

$$A(a, x_c, x) = \frac{a^2}{a^2 + (x - x_c)^2},$$

the center x_c and the width parameter a. In a linearized Boussinesq atmosphere, Skamarock and Klemp (1994) have derived an analytic solution for the potential temperature perturbation

$$\theta_{lin}(x,z,t) = \sin(lz)\Delta\theta_0 a \int_0^\infty \exp(-ka)\cos(\lambda t)\cos(xk)\,dk \tag{11}$$

with $\lambda = Nk/\sqrt{\delta_H k^2 + l^2}$ that gives a qualitative approximation to the solutions of the non-linear non-hydrostatic system as well as for the hydrostatic system in (1). Because of the dispersion relation

$$c(k) = \pm\frac{\lambda}{k} = \pm\frac{N}{\sqrt{\delta_H k^2 + l^2}} \tag{12}$$

for the Boussinesq atmosphere, we expect the fastest waves in the non-hydrostatic system case $\delta_H = 1$ to have the same speed N/l as the dispersion free waves in the hydrostatic system $\delta_H = 0$.
This test is used for two setups, in short and long atmospheric channels. In the short channel setup, we consider the spatial domain $\Omega = (0, 300\text{km}) \times (0, 10\text{km})$, the constants $x_c = 90\text{km}$, $a = 5\text{km}$ and the integration time $T = 3000\text{s}$. In the long channel setup, the domain $\Omega = (0, 6000\text{km}) \times (0, 10\text{km})$ with the constants $x_c = 1800\text{km}$, $a = 100\text{km}$ and the integration time $T = 60000\text{s}$ is used. For all experiments with the short channel setup, the anisotropic model resolution is defined by the anisotropy parameter $\beta = 1$. For the long channel setup the parameter is set to $\beta = 20$.
For the non-hydrostatic and hydrostatic Boussinesq equations, Fig. 1 depicts the potential temperature perturbation after 3000s for the short channel setup and after 60000s for the long channel setup. For the long channel, because the differences between the non-hydrostatic and hydrostatic cases are not visible, the hydrostatic plot is omitted. The numerical solutions of (2), for the potential temperature perturbation θ with $k = 1$, $h = 0.6\text{km}$, $\Delta t = \Delta t_{so}$ are given in Fig. 2. This setup yields a time step of $\Delta t = 1.1\text{s}$. Again for the long channel, no differences are visible between the non-hydrostatic and hydrostatic systems and we only plot the first one. Qualitatively, the experiments for the non-hydrostatic and hydrostatic systems are in good agreement with the Boussinesq solutions in Fig. 1; nonetheless, visible differences can be observed, especially in the vertical structure. Further, the linear dispersion property (12) is in very good agreement with the non-linear experiments. This can be seen by the dispersion for the short channel and the non-hydrostatic system with $\delta_H = 1$. For the long channel setup, the perturbation is dominated by long horizontal wave numbers and thus the wave dispersion effect is reduced. For the hydrostatic system in both channels the experiments show no significant dispersion, as expected.
For smooth solutions, the convergence properties of the discontinuous Galerkin method are studied. Given a fixed polynomial order k, the order of convergence $k + 1$ for the L^2-norm can be expected. To generate smooth solutions, the initial condition (10) has to be modified. First, the periodic boundary conditions lead to jumps along the lateral boundaries of Ω. Second, the reflecting boundary conditions on top and bottom of Ω can be reinterpreted as a vertical continuation by mirroring (10) along the horizontal axis that features jumps in the vertical derivatives of (10). Thus only for the convergence study, (10) is replaced by the smooth potential temperature perturbation

$$\theta'_{sm}(x, z) = \Delta\theta_0(1 - \cos(2lz))A(a, x_c, x)\varphi_{x_c}(x - x_c)$$

with $\varphi_\varepsilon(x) = \exp(-\frac{\varepsilon^2}{\varepsilon^2 - x^2})$ if $|x| < |\varepsilon|$ and $\varphi_\varepsilon(x) = 0$ otherwise.
The relative L^2-error η for the numerical solution θ is derived with respect to a reference solution θ_h with the model resolution h, that is

$$\eta = \eta(h, \theta) = \frac{\|\theta - \theta_h\|_{L^2(\Omega)}}{\|\theta_r + \theta_h\|_{L^2(\Omega)}}.$$

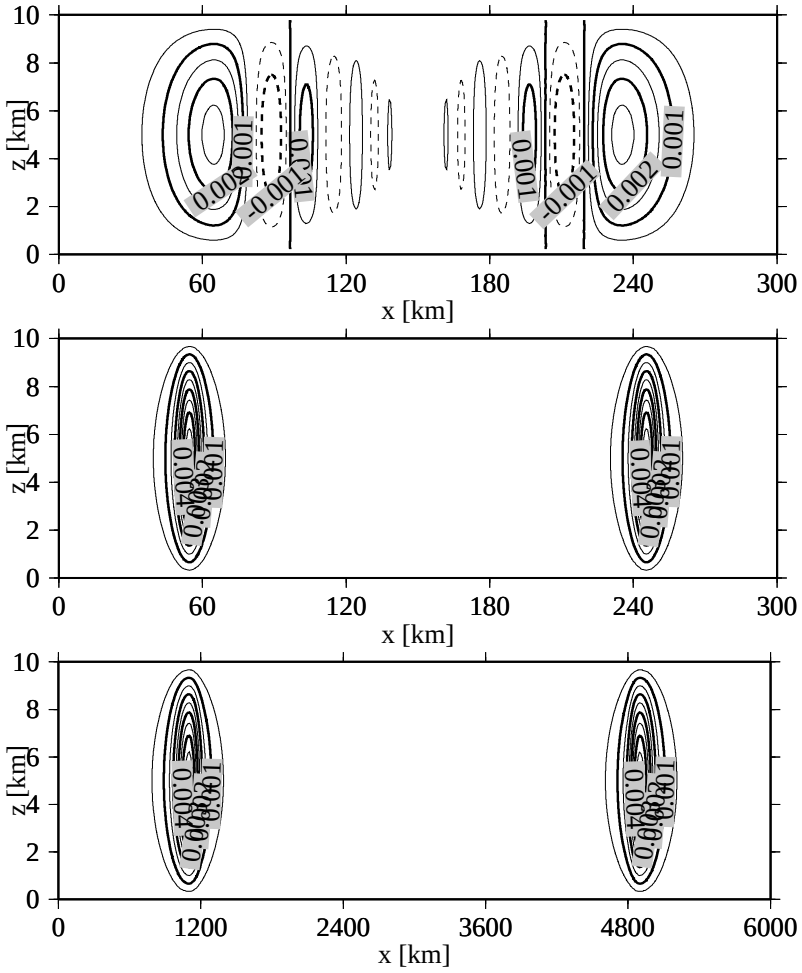

Figure 1: Gravity waves, section 4.1, potential temperature perturbation in (11) for Boussinesq equations, contour interval 5×10^{-4}K, top: short channel, $T = 3000$s, non-hydrostatic system, middle: short channel, $T = 3000$s, hydrostatic system, bottom: long channel, $T = 60000$s, non-hydrostatic system; In the long channel, the non-hydrostatic and hydrostatic plots look the same. Thus, the hydrostatic plot is omitted.

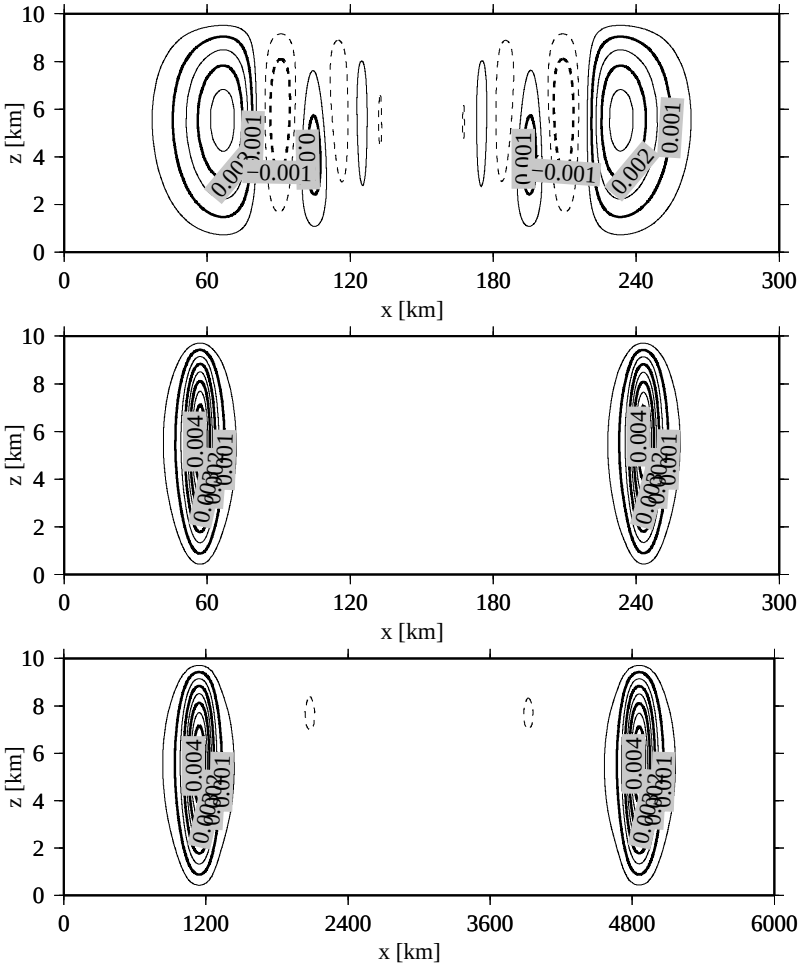

Figure 2: Gravity waves, section 4.1, model results for potential temperature perturbation θ, contour interval 5×10^{-4}K, top: short channel, $T = 3000$s, non-hydrostatic system, middle: short channel, $T = 3000$s, hydrostatic system, bottom: long channel, $T = 60000$s, non-hydrostatic system; In the long channel, the non-hydrostatic and hydrostatic plots look the same. Thus, the hydrostatic plot is omitted.

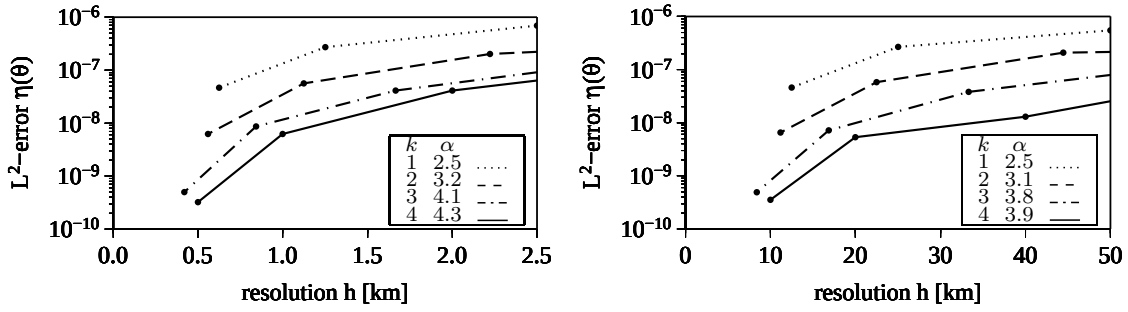

Figure 3: Gravity waves, section 4.1, L^2-errors and convergence rates for the non-hydrostatic system, $T = 300$s, BDF2, $\Delta t = \frac{1}{5}\Delta t_{so}$, left: short channel, right: long channel.

With the reference value θ_r from section 2.2 and the perturbation value θ_h, $\theta_r + \theta_h$ is the physical value for the potential temperture. Then, the convergence rate $\alpha_\theta(h,k)$ for the variable θ is defined depending on the model resolution h and the fixed polynomial order k. For that, the numerical solutions θ_h, θ_{2h}, θ_{4h} are considered with respect to the three model resolutions h, $2h$ and $4h$. Then

$$\alpha = \alpha_\theta(h,k) = \frac{\ln \eta(h,\theta_{2h}) - \ln \eta(h,\theta_{4h})}{\ln(2h) - \ln(4h)}$$

gives an approximation to the convergence order of the method.
The convergence properties of the spatial discretization are analyzed for the fixed integration time of $T = 300$s. To separate the temporal error, we seek the largest time step size for the BDF2 method such that error and convergence rates do not change for smaller time steps. For the presented experiments, this is nearly obtained for the time step $\Delta t = \frac{1}{5}\Delta t_{so}$, with Δt_{so} in (8). The relative L^2-errors η and convergence rates α are illustrated in Fig. 3 for the non-hydrostatic system in both channels. The model converges, that is the error decreases monotonously with increasing model resolution and increasing polynomial order. Furthermore for each polynomial order $k = 1, .., 4$, α is close to the expected value $k + 1$. Only for the high order case $k = 4$, α is slightly limited by the temporal error. In contrast to this, Fig. 4 shows the same errors η and rates α for non-smooth initial conditions (10) and for longer time steps, respectively. The initial conditions cause a slight degradation but the long time step strongly degrades the accuracy.
The same convergence experiments but for the hydrostatic system are depicted in Fig. 5. Again, the method converges and the convergence rates match very well with the expected values. Compared to the non-hydrostatic system, the convergence rates have even improved.

4.2 Hydrostatic Mountain Waves

Mountain waves arise in a steady-state flow perturbed by a mountain orography. This test case is comprised of a horizontal wind field u with a single hydrostatic mountain with a large horizontal size a such that the forcing frequency u/a is small

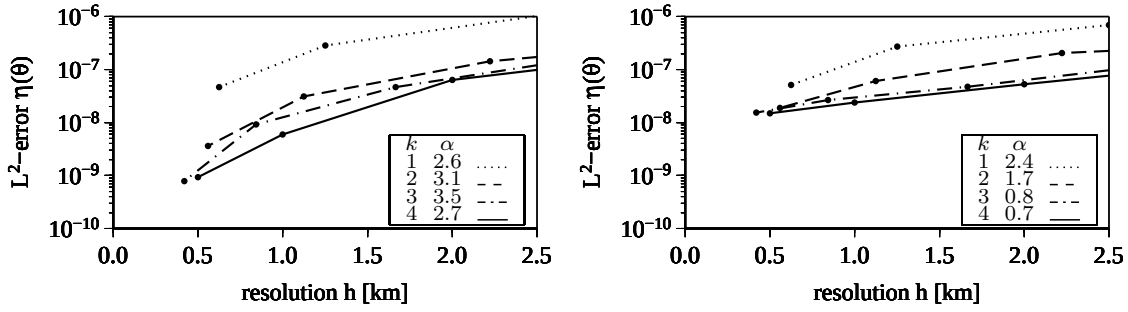

Figure 4: Gravity waves, section 4.1, L^2-errors and convergence rates for the non-hydrostatic system, short channel, $T = 300$s, BDF2, left: non-smooth initial condition (10), $\Delta t = \frac{1}{5}\Delta t_{so}$, right: smooth initial condition, $\Delta t = 5\Delta t_{so}$.

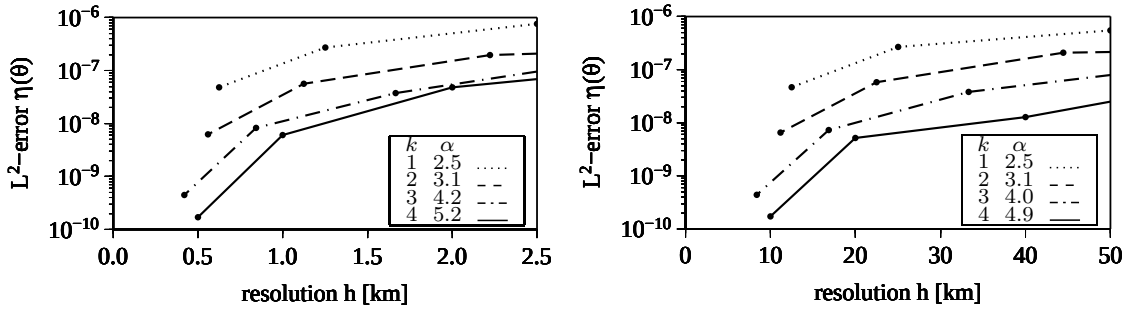

Figure 5: Gravity waves, section 4.1, L^2-errors and convergence rates for the hydrostatic system, $T = 300$s, BDF2, $\Delta t = \frac{1}{5}\Delta t_{so}$, left: short channel, right: long channel.

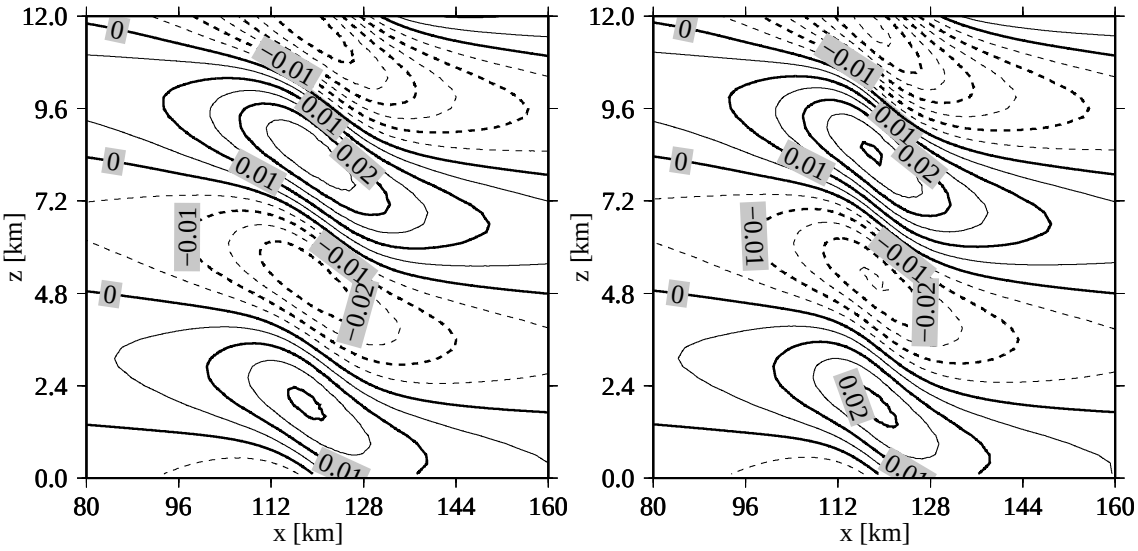

Figure 6: Hydrostatic mountain, section 4.2, horizontal velocity perturbation u, contour interval 0.005m/s, cutout of Ω, $T = 10$h, left: non-hydrostatic system, right: hydrostatic system.

compared to the Brunt-Väisälä frequency $N = g\sqrt{\kappa/RT}$. Thus, internal waves are excited and propagate freely into the vertical direction, see Smith (1979). We use the same setup as in Giraldo and Restelli (2008) which is similar to that in Pinty *et al.* (1995) and Klemp and Lilly (1978). In the spatial domain $\Omega = (0, 240\text{km}) \times (0, 20\text{km})$, an Agnesi mountain is given by

$$h(x, z) = h_0 A(a, x_c, x)$$

with $h_0 = 1$m, $x_c = 120$km and the mountain width parameter $a = 10$km. The initial condition is a hydrostatic isothermal atmosphere with $T = 250$K, $p(z = 0) = 100$kPa and the horizontal velocity $u = 20$m/s. The hydrostatic characteristics of the mountain is obtained by the relation $aN/2\pi u \gg 1$. On the bottom, reflecting boundary conditions are assumed while on the top and lateral boundaries sponge layers of 6km respectively 20km thickness are applied. The lateral sponges enforce the inflow and outflow conditions to agree with the initial data.
For both equation systems, the solution converges to a quasi-stationary state. After a simulation time of $T = 10$h, Fig. 6 depicts the horizontal velocity perturbations for $k = 1$, $h = 1.2$km, $\beta = 4.8$ and $\Delta t = 7.6$s in a cutout of Ω. For the non-hydrostatic system, the wave structure agrees very well with Restelli and Giraldo (2009). Further, the results for the large horizontal wave numbers of the mountain profile lead to a very good agreement between the non-hydrostatic and hydrostatic systems.
The convergence analysis for η and α is given in Fig. 7 for the integration time $T = 360$s and the anisotropy parameter $\beta = 1.5$. Convergence is observed for the non-hydrostatic and hydrostatic systems, but only for resolutions better than approximately 6km. The convergence rates are close to the expected values but the

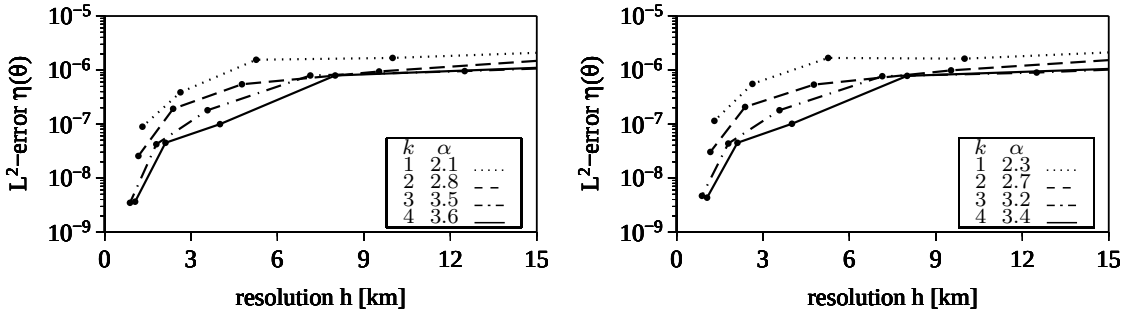

Figure 7: Hydrostatic mountain, section 4.2, L^2-errors and convergence rates, $T =$ 360s, BDF2, $\Delta t = \Delta t_{so}$, left: non-hydrostatic system, right: hydrostatic system.

higher order convergence rates ($k = 3, 4$) are reduced slightly. This effect might be attributed to the non-smooth acoustic wave fronts during the transient phase forced by the mountain.

4.3 Non-Hydrostatic Mountain Waves

Non-hydrostatic mountain waves are excited over a mountain orography with a smaller horizontal size a than in section 4.2. Here, the forcing frequency u/a is large compared to the Brunt-Väisälä frequency N such that the vertical wave propagation is damped by buoyancy forces. We study a similar test setup as in Giraldo and Restelli (2008). In the spatial domain $\Omega = (0, 100\text{km}) \times (0, 20\text{km})$, the same Agnesi mountain profile as in section 4.2 is used but with the parameters $h_0 = 1\text{m}$, $x_c =$ 50km and $a = 1\text{km}$. The initial condition is an uniformly stratified atmosphere with $N = 0.01\text{s}^{-1}$, $T(z = 0) = 280\text{K}$, $p(z = 0) = 100\text{kPa}$ and the horizontal velocity $u = 10\text{m/s}$. Now, the dimensionless parameter $aN/2\pi u \ll 1$ describes the non-hydrostatic characteristics of the mountain. The same boundary conditions as in section 4.2 are assumed, but with sponge layer thicknesses of 6km (top) and 10km (lateral). For both equation systems, after a simulation time of $T = 5\text{h}$, a quasi-stationary state is achieved. Fig. 8 depicts the horizontal velocity perturbations for $k = 1$, $h = 0.4\text{km}$, $\beta = 2$ and $\Delta t = 4.2\text{s}$ in a cutout of Ω. The wave structure for the non-hydrostatic system is in very good agreement to Restelli and Giraldo (2009). For the hydrostatic system, the amplified horizontal gradients lead to strong waves located above the orographic perturbation. Thus, the small horizontal scales of the orographic perturbation yield significant differences between the non-hydrostatic and hydrostatic systems.

The convergence analysis for η and α is given in Fig. 9 for the integration time $T = 180\text{s}$ and the anisotropy parameter $\beta = 1$. Because the horizontal mountain scale is 10 times smaller compared to section 4.2, convergence is established for the non-hydrostatic and hydrostatic systems below a model resolutions of 1km. The convergence rates are satisfactory, but below the expected theoretical rates of convergence. One reason is the non-smoothness of the solution, as described in section 4.2. Another reason could be the limited spatial resolution which reduces the confidence in the values of the estimated convergence rates α.

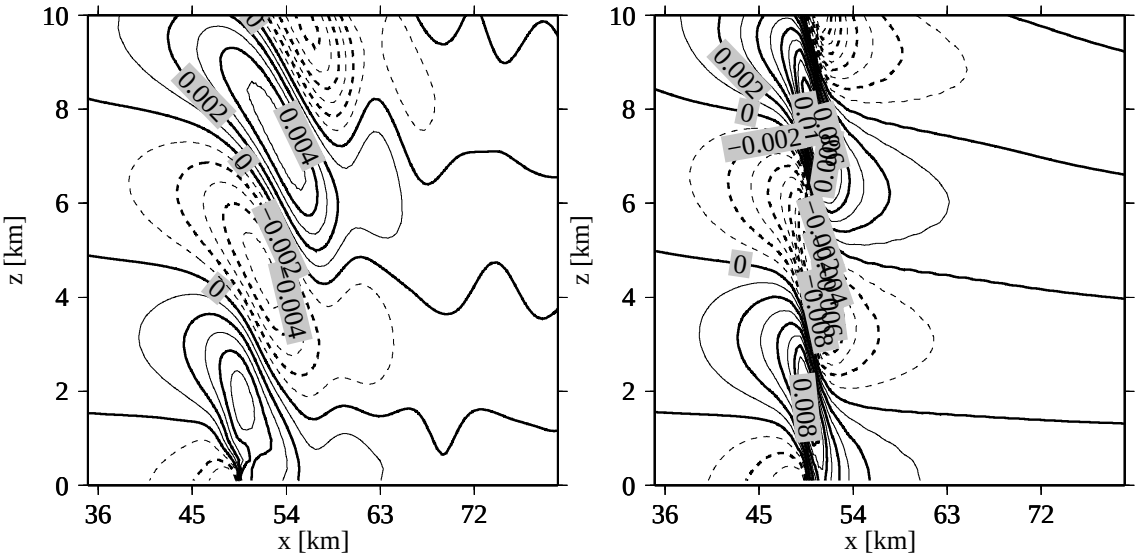

Figure 8: Non-hydrostatic mountain, section 4.3, horizontal velocity perturbation u, contour interval 0.001m/s, cutout of Ω, $T = 5$h, left: non-hydrostatic system, right: hydrostatic system.

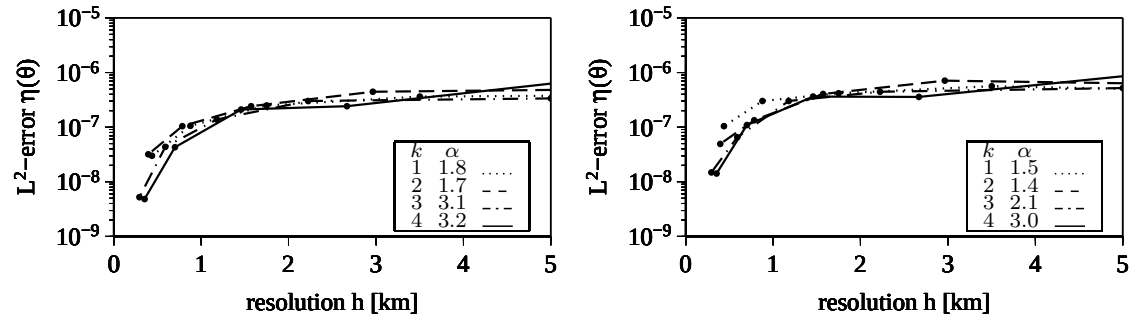

Figure 9: Non-hydrostatic mountain, section 4.3, L^2-errors and convergence rates, $T = 180$s, BDF2, $\Delta t = \Delta t_{so}$, left: non-hydrostatic system, right: hydrostatic system.

This section and section 4.2 allow the conclusion that the hydrostatic equation system is able to model mountain waves very good above the horizontal mountain scale of approximately 10km. In contrast to that, finer mountain scales lead to artificial wave propagation. One possibility to prevent this error in a hydrostatic model is to apply the model with a resolution above the 10km scale. Finer model resolutions are appropriate only if the horizontal mountain scale is still above the 10km scale.

4.4 Schär Mountain Waves

An experiment constituting a superposition of hydrostatic and non-hydrostatic mountain waves is described in Schär *et al.* (2002). The orography is given by

$$h(x) = h_0 \exp\left(-\frac{(x-x_c)^2}{a^2}\right) \cos^2\left(\frac{\pi(x-x_c)}{\lambda}\right)$$

with the mountain height $h_0 = 250\text{m}$, $x_c = 25\text{km}$ and the wave parameters $a = 5\text{km}$ and $\lambda = 4\text{km}$. In the spatial domain $\Omega = (0, 50\text{km}) \times (0, 20\text{km})$ for the initial and reference fields an uniformly stratified atmosphere is assumed with $N = 0.01\text{s}^{-1}$, $T(z=0) = 280\text{K}$, $p(z=0) = 100\text{kPa}$ and the horizontal velocity $u = 10\text{m/s}$. The same boundary condition as in the previous sections are used. The top and lateral sponge layer thicknesses are 6km and 5km, respectively.
For the non-hydrostatic system after a simulation time of $T = 10\text{h}$, the quasi-stationary horizontal velocity perturbations are plotted in Fig. 10 for $k = 2$, $h = 0.2\text{km}$, $\beta = 0.5$ and $\Delta t = 1.9\text{s}$. Following the discussion in section 4.3 about small scale mountains in the hydrostatic system, here the hydrostatic results are omitted. Like in section 4.2 qualitatively this result is in good agreement to Schär *et al.* (2002) and Restelli and Giraldo (2009). Small and large scale waves are apparent, the larger-scale waves propagate and the smaller-scale waves rapidly decay with height.
The results of the convergence studies for the non-hydrostatic system is given in the right column of Fig. 10 for the integration time $T = 360\text{s}$ and the anisotropy parameter $\beta = 1$. Qualitatively here, the convergence results are similar to that in section 4.3. Convergence is obtained below a model resolution of 1km. More so than in sections 4.2 and 4.3, there is a significant difference between the observed convergence rates and their expected values.

5 Summary

The article presents a 2-dimensional mesoscale model of the atmosphere based on the non-hydrostatic system and its hydrostatic approximation. Both systems are discretized with a discontinuous Galerkin method in space respecting a logically rectangular terrain following grid. We present an unified formulation of non-hydrostatic and hydrostatic atmospheric systems using a mathematically consistent discontinuous Galerkin formulation; the introduction of a specialized flux function is one of two keys to the success of this approach. To avoid small time steps respecting a severe

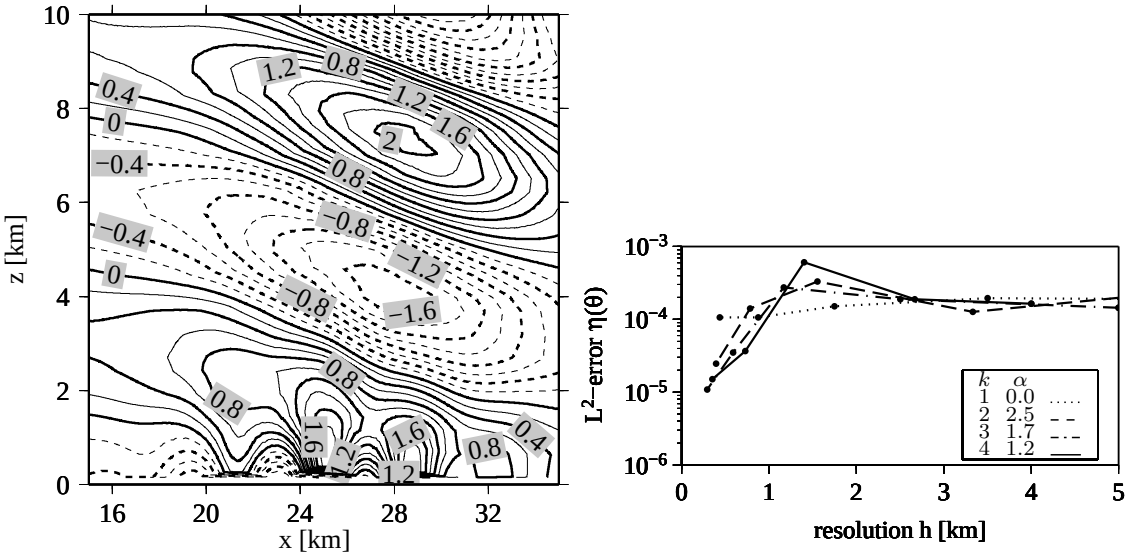

Figure 10: Schär Mountain, Section 4.4, non-hydrostatic system, left: horizontal velocity perturbation u, contour interval 0.2m/s, $T = 10$h, right: L^2-errors and convergence rates, $T = 360$s, BDF2, $\Delta t = \Delta t_{so}$.

CFL-condition a semi-implicit linear multi-step method in time has been applied. The time step size is controlled according to a heuristic CFL-condition respecting the grid size and the polynomial order of the method. The second key concept in constructing an unified non-hydrostatic/hydrostatic discontinuous Galerkin relies on a semi-implicit time-integration method whereby the hydrostatic constraint is imposed implicitly as part of the time-integration strategy.
The validation experiments show correct wave propagation properties as well as the expected convergence rates. The gravity wave propagation experiments show good agreement with the analytic solution of the linearized Boussinesq atmosphere. Specifically, wave dispersion for the non-hydrostatic system and no dispersion for the hydrostatic system are observed. With smooth initial conditions, high order convergence rates Δx^{k+1} are observed for polynomial orders $k = 1, ..., 4$. For the non-hydrostatic and hydrostatic systems, the results for the linear hydrostatic mountain waves qualitatively agree. For the non-hydrostatic system, the result for the linear non-hydrostatic mountain waves are qualitatively correct. As expected, qualitatively the results of the hydrostatic system are different. Because the horizontal size of the Schär mountains are in the non-hydrostatic scale, differences between both systems are expected and are indeed shown to differ. The non-hydrostatic system gives the well known wave propagation structure. Although the experiments show convergence for all mountain wave experiments, the convergence rates are below the expected theoretical order. Only, the non-hydrostatic system for the hydrostatic mountain test gives the convergence order Δx^{k+1} for $k = 1, 2$.
For 2-dimensional physical problems, like the study of mountain wave propagation, the presented model is already an appropriate tool. But for more realistic mesoscale applications, a 3-dimensional model is required. This could be achieved generalizing

the present code to 3-dimensional grids based on cubic or prismatic grid elements. This work has already begun and we shall report our findings for more complicated flow problems in the future, perhaps including moist physics, and other basisc physical parameterizations.

Acknowledgements

The first author (M.L.) thanks the German Research Foundation for providing partial support through the funding number LA2455/1-1. The second author (F.X.G) gratefully acknowledges the support of the Office of Naval Research through program element PE-0602435N. The authors M.L., F.X.G. and M.R. thank the Office of Naval Research for providing partial support for M.L. and M.R. through the Visiting Scientist Program.

References

Biswas R, Devine K, Flaherty J. 1994. Parallel, adaptive finite element methods for conservation laws. *Appl. Numer. Math.* **14**: 225–283.

Bos L, Taylor M, Wingate B. 2000. Tensor product Gauss-Lobatto points are Fekete points for the cube. *Mathematics of Computation* **70**(236): 1543–1547.

Cockburn B, Shu CW. 2001. Runge-Kutta discontinuous Galerkin methods for convection-dominated problems. *J. Sci. Comput.* **16**: 173–261.

Dolejsi V, Feistauer M. 2004. A semi-implicit discontinuous Galerkin finite element method for the numerical solution of inviscid compressible flow. *J. Comput. Phys.* **198**: 727–746.

Durran D. 1989. Improving the anelastic approximation. *J. Atmos. Sci.* **46**: 1453–1461.

Gal-Chen T, Somerville R. 1975. On the Use of a Coordinate Transformation for the Solution of the Navier-Stokes Equations. *J. Comput. Phys.* **17**: 209–228.

Giraldo F. 2005. Semi-implicit time-integrators for a scalable spectral element atmospheric model. *Q. J. R. Meteorol. Soc.* **131**: 2431–2454.

Giraldo F. 2006. High-order triangle-based discontinuous Galerkin methods for hyperbolic equations on a rotating sphere. *J. Comput. Phys.* **214**: 447–465.

Giraldo F, Hesthaven JS, Warburton T. 2002. Nodal high-order discontinuous Galerkin methods for the spherical shallow water equations. *J. Comput. Phys.* **181**: 499–525.

Giraldo F, Restelli M. 2008. A study of spectral element and discontinuous Galerkin methods for the Navier-Stokes equations in nonhydrostatic mesoscale atmospheric modeling: Equation sets and test cases. *J. Comput. Phys.* **227**: 3849–3877.

Giraldo F, Restelli M. 2009. High-order semi-implicit time-integration of a triangular discontinuous Galerkin oceanic shallow water model. *Int. J. Numer. Meth. Fluids* Submitted.

Giraldo F, Restelli M, Läuter M. 2009. Semi-implicit formulations of the Navier-Stokes equations: application to nonhydrostatic atmospheric modeling. *SIAM J. Sci. Comput.* Submitted.

Hundsdorfer W, Verwer J. 2003. *Numerical solution of time-dependent advection-diffusion-reaction equations*. Springer.

Kalnay E. 2003. *Atmospheric modeling, data assimilation and predictablity*. Cambridge University Press.

Kanevsky A, Carpenter M, Gottlieb D, Hesthaven J. 2007. Application of implicit-explicit high order Runge-Kutta methods to discontinuous-Galerkin schemes. *J. Comput. Phys.* **225**: 1753–1781.

Klemp J, Lilly D. 1978. Numerical simulation of hydrostatic waves. *J. Atmos. Sci.* **35**: 78–107.

Klöckner A, Warburton T, Bridge J, Hesthaven J. 2009. Nodal discontinuous galerkin methods on graphics processors. *J. Comput. Phys.* **228**: 7863–7882.

Läuter M, Giraldo F, Handorf D, Dethloff K. 2008. A discontinuous Galerkin method for the shallow water equations in spherical triangular coordinates. *J. Comput. Phys.* **227**(24): 10 226–10 242.

Nair RD, Thomas SJ, Loft RD. 2005. A discontinuous Galerkin global shallow water model. *Mon. Wea. Rev.* **133**: 876–888.

Ogura Y, Phillips N. 1962. Scale analysis of deep and shallow convection in the atmosphere. *J. Atmos. Sci.* **19**: 173–179.

Pinty JP, Benoit R, Richard E, Laprise R. 1995. Simple tests of a semi-implicit semi-Lagrangian model on 2d mountain wave problems. *Mon. Wea. Rev.* **123**: 3042–3058.

Reed W, Hill T. 1973. Triangular mesh methods for the neutron transport equation. Technical Report LA-UR-73-479, Los Alamos Scientific Laboratory.

Restelli M, Giraldo F. 2009. A conservative discontinuous Galerkin sem-implicit formulation for the Navier-Stokes equations in nonhydrostatic mesoscale modeling. *SIAM J. Sci. Comput.* **31**: 2231–2257.

Schär C, Leuenberger D, Fuhrer O, Lüthi D, Girard C. 2002. A new terrain-following vertical coordinate formulation for atmospheric prediction models. *Mon. Wea. Rev.* **130**: 2459–2480.

Skamarock W, Klemp J. 1994. Efficiency and accuracy of the Klemp-Wilhelmson time-splitting technique. *Mon. Wea. Rev.* **122**: 2623–2630.

Smith R. 1979. The influence of mountains on the atmosphere. *Advances in Geophysics* **21**: 87–230.